

# Single-atom catalyst for high-performance methanol oxidation

Zhiqi Zhang <sup>1,6</sup>, Jiapeng Liu <sup>1,6</sup>, Jian Wang <sup>2,6</sup>, Qi Wang<sup>3</sup>, Yuhao Wang<sup>1</sup>, Kai Wang<sup>4</sup>, Zheng Wang <sup>1</sup>, Meng Gu <sup>3</sup>, Zhenghua Tang <sup>4</sup>, Jongwoo Lim <sup>2</sup>, Tianshou Zhao <sup>1</sup> & Francesco Ciucci <sup>1,5</sup>✉

Single-atom catalysts have been widely investigated for several electrocatalytic reactions except electrochemical alcohol oxidation. Herein, we synthesize atomically dispersed platinum on ruthenium oxide (Pt<sub>1</sub>/RuO<sub>2</sub>) using a simple impregnation-adsorption method. We find that Pt<sub>1</sub>/RuO<sub>2</sub> has good electrocatalytic activity towards methanol oxidation in an alkaline media with a mass activity that is 15.3-times higher than that of commercial Pt/C (6766 vs. 441 mA mg<sup>-1</sup>Pt). In contrast, single atom Pt on carbon black is inert. Further, the mass activity of Pt<sub>1</sub>/RuO<sub>2</sub> is superior to that of most Pt-based catalysts previously developed. Moreover, Pt<sub>1</sub>/RuO<sub>2</sub> has a high tolerance towards CO poisoning, resulting in excellent catalytic stability. Ab initio simulations and experiments reveal that the presence of Pt–O<sub>3f</sub> (3-fold coordinatively bonded O)–Ru<sub>cus</sub> (coordinatively unsaturated Ru) bonds with the undercoordinated bridging O in Pt<sub>1</sub>/RuO<sub>2</sub> favors the electrochemical dehydrogenation of methanol with lower energy barriers and onset potential than those encountered for Pt–C and Pt–Ru.

<sup>1</sup>Department of Mechanical and Aerospace Engineering, The Hong Kong University of Science and Technology, Hong Kong, China. <sup>2</sup>Department of Chemistry, College of Science, Seoul National University, Seoul, South Korea. <sup>3</sup>Department of Materials Science and Engineering, Guangdong Provincial Key Laboratory of Energy Materials for Electric Power, Southern University of Science and Technology, Shenzhen, China. <sup>4</sup>Guangzhou Key Laboratory for Surface Chemistry of Energy Materials and New Energy Research Institute, School of Environment and Energy, South China University of Technology, Guangzhou Higher Education Mega Centre, Guangzhou, China. <sup>5</sup>Department of Chemical and Biological Engineering, The Hong Kong University of Science and Technology, Hong Kong, China. <sup>6</sup>These authors contributed equally: Zhiqi Zhang, Jiapeng Liu, Jian Wang. ✉email: [francesco.ciucci@ust.hk](mailto:francesco.ciucci@ust.hk)

Platinum is the most effective element for anodic methanol oxidation reaction (MOR) in direct methanol fuel cells<sup>1,2</sup>. The electrocatalytic activity of Pt is highly dependent on its geometrical structure and the surrounding environment<sup>1</sup>. To improve MOR activity and reduce Pt loading, conventional strategies have focused on<sup>2</sup> (i) tailoring the structure and/or morphology of Pt (e.g., by making hollow/framed<sup>3</sup> or core-shelled<sup>4</sup> Pt); and (ii) hybridizing Pt with other elements (e.g., Co<sup>3</sup>, Ni<sup>5</sup>, Sn<sup>6</sup>, Bi<sup>7</sup>, etc.). However, the Pt in these catalysts is usually assembled as a nanoparticle of diameter greater than 1 nm, leading to unsatisfactory mass activity. Furthermore, in MOR, Pt nanoparticles are susceptible to poisoning by adsorbed intermediates (CO<sub>ads</sub>)<sup>5</sup>, resulting in activity loss. Hence, developing new types of Pt-based MOR electrocatalysts with high activity and anti-poisoning capability is of both practical and fundamental significance.

Single-atom catalysts (SACs) are now emerging as a new class of catalysts with extraordinary activity towards many electrocatalytic reactions, including oxygen and hydrogen evolution, oxygen, CO<sub>2</sub>, and N<sub>2</sub> reduction, and hydrogen and formic acid oxidation<sup>8–12</sup>. Pt SACs have utmost utilization of Pt atoms and good capability for CO oxidation<sup>13</sup>. However, the electrochemical dehydrogenation of methanol to CO in MOR requires at least three contiguous Pt atoms<sup>14</sup>. Further, it has been reported that SACs consisting of Pt single atoms supported on carbon nanotubes are inactive towards MOR<sup>15</sup>. Yet, we should note that these studies focused only on the Pt active centers rather than the entire catalysts, thereby neglecting the environment surrounding Pt. In this regard, enhancing the activity of single atomic Pt towards MOR is a scientifically significant and challenging topic.

For SACs, the atomic coordination of single atoms also plays an important role in determining the catalytic activity<sup>16</sup>. It has been shown that the electronic structure and coordination of the central single atoms can be adjusted by tuning the bonds between the single atoms and the substrate<sup>17–20</sup>. Herein, we designed two types of Pt SACs. Thanks to a simple adsorption–impregnation preparation method<sup>21</sup>, single Pt atoms were immobilized on RuO<sub>2</sub> and carbon black (VXC-72) to obtain Pt<sub>1</sub>/RuO<sub>2</sub> and Pt<sub>1</sub>/VXC-72, respectively. The Pt<sub>1</sub>/RuO<sub>2</sub> SACs showed superb mass activity (6766 mA mg<sup>-1</sup><sub>Pt</sub>) and stability towards the MOR, far superior to those of most Pt-based catalysts developed to date. The MOR mechanism including the dehydrogenation of methanol and CO electrooxidation is further studied by density functional theory (DFT), confirming the experimental observation that the prepared SACs are active for the alcohol oxidation reaction. This finding suggests an approach of SACs for direct alcohol fuel cells.

## Results

**Structure characterization of Pt<sub>1</sub>/RuO<sub>2</sub>.** RuO<sub>2</sub> and VXC-72 supports were characterized by transmission electron microscopy (TEM), X-ray photoelectron spectroscopy (XPS), and X-ray diffraction (XRD) (Supplementary Fig. 1). Pt<sub>1</sub>/RuO<sub>2</sub> and Pt<sub>1</sub>/VXC-72 catalysts with an identical Pt loading of 0.38 wt% were prepared by simple impregnation/adsorption followed by filtration and washing (for more details, see ‘Methods’ and Supplementary Fig. 2). Figure 1 shows the catalysts’ morphology and structure. As revealed by the bright spots marked as yellow circles in the high-angle annular dark-field (HAADF) scanning transmission electron microscopy (STEM) image, individual Pt atoms were randomly dispersed on RuO<sub>2</sub> (Fig. 1a). The magnified HAADF-STEM image of Pt<sub>1</sub>/RuO<sub>2</sub> suggests that the Pt atoms exactly substituted Ru (Fig. 1b). The presence of Pt single atoms was further verified by the intensity profile along with the dashed rectangle in the image (the inset in Fig. 1b), where the Pt atom

brightness is more intense than that of Ru due to the higher Z number. The corresponding elemental mapping shows that Pt, Ru, and O were homogeneously distributed throughout the entire Pt<sub>1</sub>/RuO<sub>2</sub> sample (Fig. 1d–g). For Pt<sub>1</sub>/VXC-72, Pt atoms were also atomically dispersed, as shown in the HAADF-STEM image (Fig. 1c). No Pt clusters/nanoparticles on VXC-72 were observed by low-magnification HAADF-STEM and TEM imaging (Supplementary Fig. 3). Due to the single-atom structure and low Pt loading, Pt peaks were, however, not detectable by XRD (Supplementary Fig. 4).

To study the coordination and electronic configuration of Pt single atoms in the Pt<sub>1</sub>/RuO<sub>2</sub> and Pt<sub>1</sub>/VXC-72, X-ray absorption fine structure (XAFS) spectroscopy and XPS were carried out (Fig. 2). The normalized X-ray absorption near-edge structure (XANES) spectra of Pt<sub>1</sub>/RuO<sub>2</sub> shows stronger white-line intensity at 11,568 eV compared to the Pt foil, suggesting that Pt is positively charged in Pt<sub>1</sub>/RuO<sub>2</sub> due to the electron transfer from Pt to the surrounding O atoms in the RuO<sub>2</sub> support (Fig. 2a)<sup>22,23</sup>. The Pt<sub>1</sub>/VXC-72 catalyst is characterized by a similar Pt-to-VXC-72 electron transfer. However, the white-line peaks suggest that the Pt in Pt<sub>1</sub>/VXC-72 has a lower charge state than the one observed for Pt<sub>1</sub>/RuO<sub>2</sub>. The average Pt oxidation numbers in Pt<sub>1</sub>/RuO<sub>2</sub> and Pt<sub>1</sub>/VXC-72 are estimated to be +2.90 and +1.22, respectively, by integrating the XANES spectra (Supplementary Fig. 5)<sup>10,24</sup>. The different charge of Pt in RuO<sub>2</sub> and VXC-72 is likely a result of the different coordination. As revealed by the *k*<sup>3</sup>-weighted extended XAFS (EXAFS) at the Pt L<sub>3</sub>-edge, no peak at 2.64 Å from Pt–Pt is observed for either Pt<sub>1</sub>/RuO<sub>2</sub> or Pt<sub>1</sub>/VXC-72, indicating full atomic dispersion for both catalysts (Fig. 2b), consistent with the HAADF-STEM images. Specifically, the R-space spectrum of Pt in Pt<sub>1</sub>/RuO<sub>2</sub> has a dominant peak at 1.62 Å from Pt–O coordination, in agreement with the PtO<sub>2</sub> case (Fig. 2b)<sup>22,23</sup>. In contrast, the dominant peak of Pt<sub>1</sub>/VXC-72 shifted to 1.83 Å (Fig. 2b). To determine the coordination of Pt in both catalysts, the main R-space peaks were fitted against corresponding models (see ‘Computational details’) by Fourier transform. For Pt<sub>1</sub>/RuO<sub>2</sub>, the coordination number of Pt–O is estimated to be 4 with an average bond length of 1.99 Å (Supplementary Fig. 6 and Supplementary Table 1). For Pt<sub>1</sub>/VXC-72, the Pt–C bond coordination number is 3, and the average bond length is 1.93 Å (Supplementary Fig. 6 and Supplementary Table 1). Also, the wavelet-transform plots of Pt<sub>1</sub>/RuO<sub>2</sub> and Pt<sub>1</sub>/VXC-72 show a maximum at ~7.5 Å<sup>-1</sup> corresponding to the Pt–O/C bonds (Fig. 2c). No intensity maximum at ~12.5 Å<sup>-1</sup> corresponding to the presence of Pt–Pt bonds was observed for either catalyst, consistent with the EXAFS (Fig. 2c).

The RuO<sub>2</sub> support contains Ru 4s with the binding energy at the range of ~70–85 eV (Supplementary Figs. 1b and 7), which is very close to the XPS signature of Pt 4f. Therefore, the Pt<sub>1</sub>/RuO<sub>2</sub> XPS peaks in the ~68–82 eV range were deconvoluted into Ru 4s and Pt 4f, i.e., Pt 4f<sub>7/2</sub> and Pt 4f<sub>5/2</sub> (Fig. 2d). The binding energies of the Pt 4f were measured to be 73.6 and 76.9 eV for Pt<sub>1</sub>/RuO<sub>2</sub>, and 72.9 and 76.2 eV for Pt<sub>1</sub>/VXC-72. The higher binding energy of Pt<sub>1</sub>/RuO<sub>2</sub> compared to Pt<sub>1</sub>/VXC-72 implies that Pt in Pt<sub>1</sub>/RuO<sub>2</sub> has a higher oxidation state, in agreement with the XANES results. Moreover, the O 1s spectrum of bare RuO<sub>2</sub> was deconvoluted into three characteristic peaks at 529.3, 530.2, and 532.3 eV (Fig. 2e), which can be attributed to M–O, M–OH, and adsorbed oxygen, respectively<sup>25</sup>. After the incorporation of Pt single atoms into RuO<sub>2</sub>, the O 1s of Pt<sub>1</sub>/RuO<sub>2</sub> shows a new peak at 531.3 eV. This peak can be attributed to the appearance of oxygen vacancies on the surface resulting from Pt single atoms (Supplementary Fig. 8)<sup>22,26</sup>. These data support the existence of Pt–O in Pt<sub>1</sub>/RuO<sub>2</sub>, in agreement with the XANES characterization. In addition, the O 1s of Pt<sub>1</sub>/VXC-72 is similar to that of

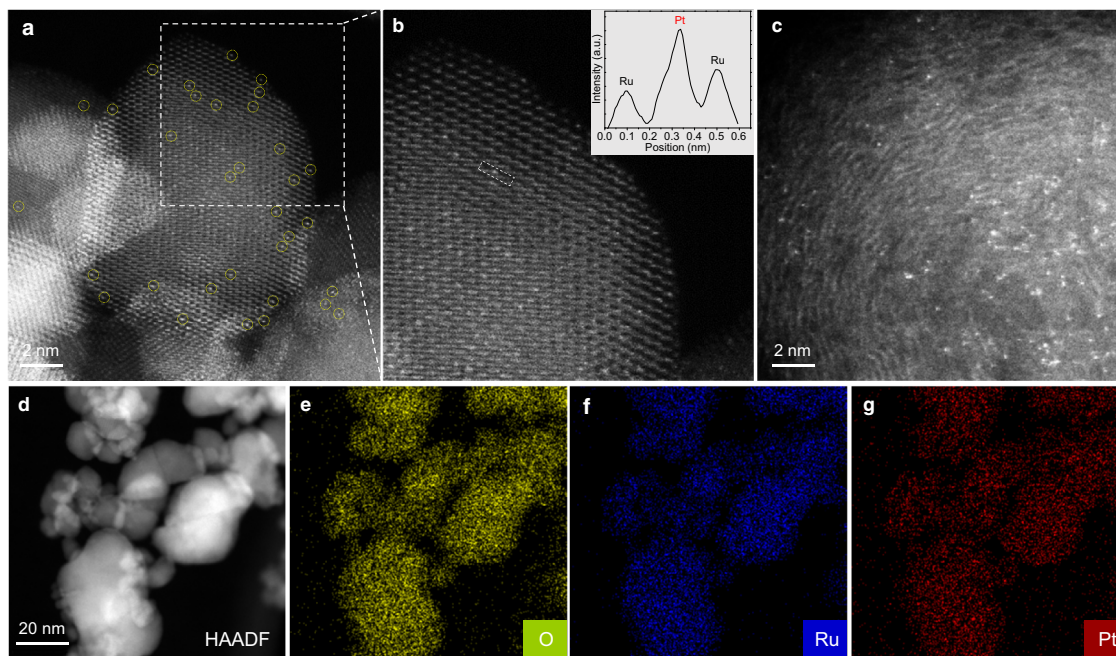


**Fig. 1** Morphological and elemental characterization of  $\text{Pt}_1/\text{RuO}_2$  and  $\text{Pt}_1/\text{VXC-72}$ . **a, b** Representative HAADF-STEM images of  $\text{Pt}_1/\text{RuO}_2$ . Inset in **(b)** is the intensity profile along with the dashed rectangle. **c** Representative HAADF-STEM image of  $\text{Pt}_1/\text{VXC-72}$ . **d-g** EDS-mapping images of  $\text{Pt}_1/\text{RuO}_2$ .

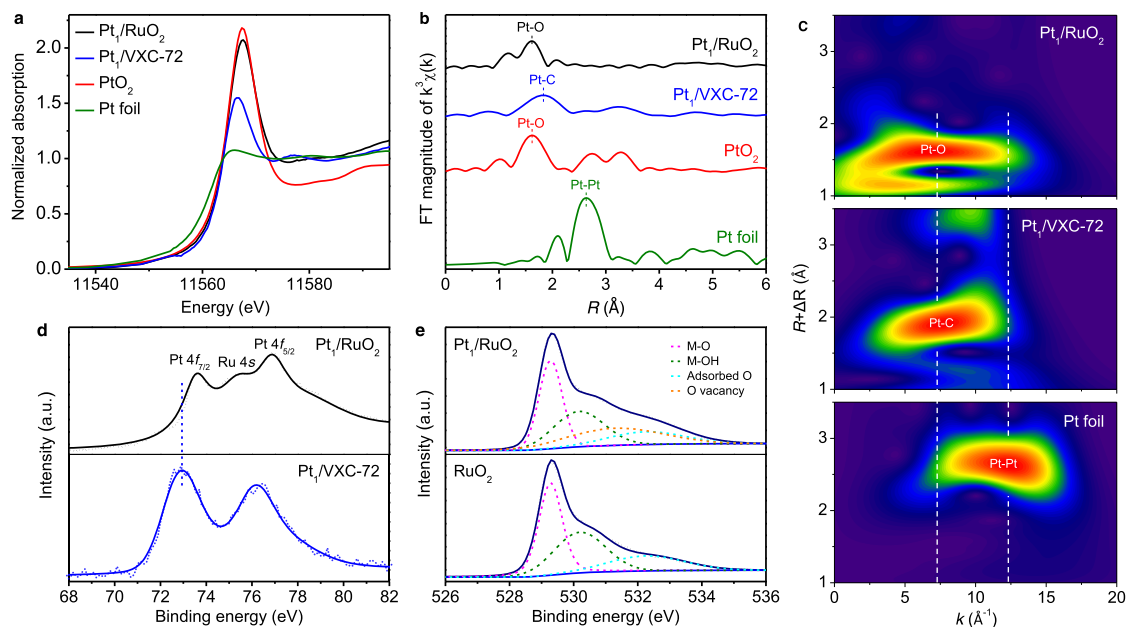


**Fig. 2** Structural characterization of  $\text{Pt}_1/\text{RuO}_2$  and  $\text{Pt}_1/\text{VXC-72}$  by XAFS and XPS. **a** Normalized XANES spectra at the Pt  $L_3$ -edge. **b**  $k^3$ -weighted R-space Fourier transformed spectra from EXAFS. **c** Wavelet transforms from experimental data. **d** XPS spectra for Pt  $4f$  and Ru  $4s$ . **e** XPS spectra for O  $1s$ . In panels **(a-c)** and **(e)**, the corresponding data for Pt foil,  $\text{PtO}_2$ , and  $\text{RuO}_2$  are presented for comparison.

VXC-72 (Supplementary Fig. 9), indicating that there is no Pt-O interaction in  $\text{Pt}_1/\text{VXC-72}$ . In other words, Pt-C coordination is dominant in  $\text{Pt}_1/\text{VXC-72}$ .

The preceding results indicate that Pt is atomically dispersed on both  $\text{RuO}_2$  and VXC-72 but surrounded by distinct coordination environments. Pt-O coordination characterizes in  $\text{Pt}_1/\text{RuO}_2$ . In contrast, Pt-C coordination is dominant in  $\text{Pt}_1/\text{VXC-72}$ .

**MOR electrocatalytic activity.** Although Pt-based nanoparticles have been the most efficient catalysts for MOR, individual Pt

atoms on carbon support are inactive towards that reaction<sup>27</sup>. By replacing the carbon support with  $\text{RuO}_2$ , the coordination of Pt single atoms changes. Herein, we evaluated in the  $\text{N}_2$ -saturated  $0.1 \text{ mol L}^{-1}$  KOH and  $1 \text{ mol L}^{-1}$  methanol solution the MOR performance of the  $\text{Pt}_1/\text{RuO}_2$  SACs. Concomitantly, these materials were compared to  $\text{Pt}_1/\text{VXC-72}$  and commercial Pt/C, see Fig. 3. As revealed by cyclic voltammogram (CV) of  $\text{Pt}_1/\text{VXC-72}$  SACs, no electrocatalytic peak was detected, indicating that  $\text{Pt}_1/\text{VXC-72}$  is inactive towards MOR (Fig. 3a). We also prepared a  $\text{Pt}_1/\text{VXC-72}$  catalyst with a higher Pt loading of 1.48 wt%, i.e., Pt/VXC-72-1.48, which had a negligible MOR activity

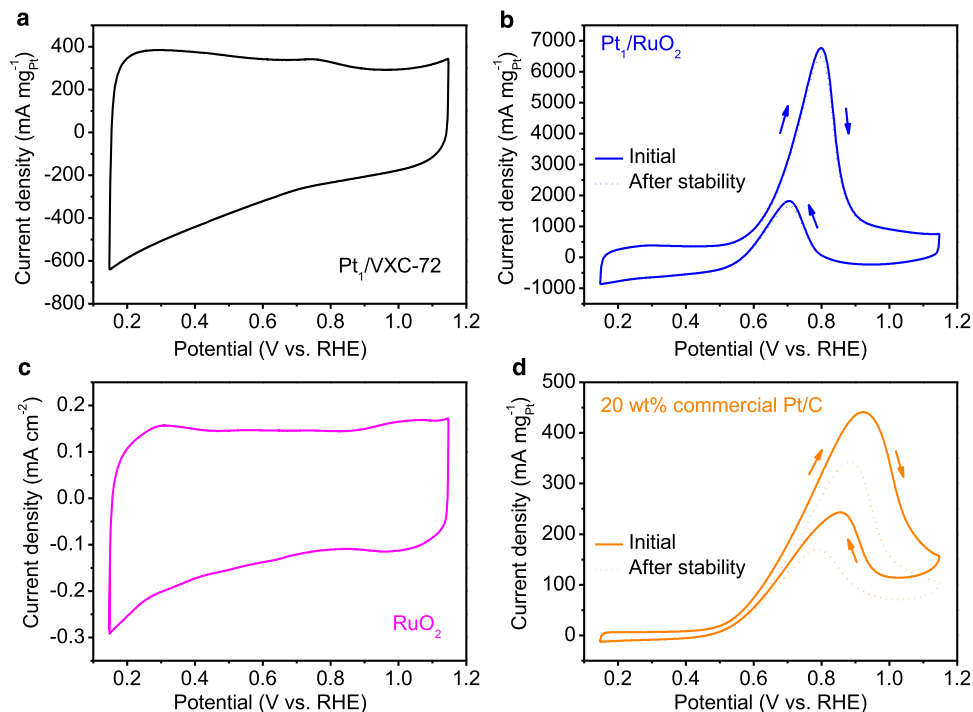


**Fig. 3** MOR performance of Pt<sub>1</sub>/RuO<sub>2</sub> and control samples in 0.1 mol L<sup>-1</sup> KOH and 1 mol L<sup>-1</sup> methanol solution at a scan rate of 50 mV s<sup>-1</sup>. **a** Pt<sub>1</sub>/VXC-72. **b** Pt<sub>1</sub>/RuO<sub>2</sub>. **c** RuO<sub>2</sub>. **d** 20 wt% commercial Pt/C.

(Supplementary Fig. 10). These results support the literature findings that single atoms or even clusters of Pt on carbon are MOR inactive. Unexpectedly, the CV curves of Pt<sub>1</sub>/RuO<sub>2</sub> SACs displayed oxidation current peaks in both the forward and backward CV scans (Fig. 3b), corresponding to methanol and intermediate products oxidation, respectively<sup>7</sup>. In contrast, the CV scan of the RuO<sub>2</sub> was featureless (Fig. 3c). Further, oxygen vacancies on the RuO<sub>2</sub> surface could not contribute to MOR (Supplementary Fig. 11). These results suggest that its MOR activity was due to having Pt single atoms on RuO<sub>2</sub>. The Pt mass activity of Pt<sub>1</sub>/RuO<sub>2</sub> was 6766 mA mg<sup>-1</sup><sub>Pt</sub> at 0.80 V vs. RHE (reversible hydrogen electrode), which is about 15.3 times higher than that of the commercial 20 wt% Pt/C (441 mA mg<sup>-1</sup><sub>Pt</sub> at 0.92 V vs. RHE) (Fig. 3b, d) and significantly larger than the data for the reported catalysts to date (Supplementary Table 2). The peak current ratio between the forward (*I<sub>f</sub>*) and backward (*I<sub>b</sub>*) scan can be used to demonstrate the CO<sub>ads</sub> tolerance<sup>28</sup>. The *I<sub>f</sub>*/*I<sub>b</sub>* of Pt<sub>1</sub>/RuO<sub>2</sub> (3.67) is more than twice that of Pt/C (1.81), suggesting an enhanced anti-poisoning ability for Pt<sub>1</sub>/RuO<sub>2</sub>. Long-term durability is another important criterion to assess the quality of a catalyst<sup>5</sup>. The stability of the Pt<sub>1</sub>/RuO<sub>2</sub> SACs and 20 wt% commercial Pt/C was evaluated by chronoamperometry at -0.1 V (vs. Ag/AgCl). After 10 h, the Pt<sub>1</sub>/RuO<sub>2</sub> mass activity remained at 6463 mA mg<sup>-1</sup><sub>Pt</sub> with a slight degradation of 4.5% (Fig. 3b). In contrast, commercial Pt/C exhibited an ~22% decrease in mass activity (344 mA mg<sup>-1</sup><sub>Pt</sub>) (Fig. 3d). After the stability test, the Pt atoms in Pt<sub>1</sub>/RuO<sub>2</sub> were isolated on the RuO<sub>2</sub> support while the Pt nanoparticles in commercial 20 wt% Pt/C were aggregated (Supplementary Figs. 12 and 13).

To reveal the origin of MOR activity, several control samples were used, see Fig. 4. In the first set of samples denoted as Pt<sub>1</sub>/RuO<sub>2</sub>-500 and Pt<sub>1</sub>/RuO<sub>2</sub>-700, Pt<sub>1</sub>/RuO<sub>2</sub> was annealed in air at 500 and 700 °C, respectively. After heat treatment, Pt single atoms on RuO<sub>2</sub> were aggregated into nanoparticles with a 1–2 nm diameter for Pt<sub>1</sub>/RuO<sub>2</sub>-500, or even 30 nm diameter for Pt<sub>1</sub>/RuO<sub>2</sub>-700 (Supplementary Fig. 14 and Fig. 4a, b), respectively. When characterized by CV, Pt/RuO<sub>2</sub>-500 showed a mass activity

of 2140 mA mg<sup>-1</sup><sub>Pt</sub>, a value lower than the 6766 mA mg<sup>-1</sup><sub>Pt</sub> of Pt<sub>1</sub>/RuO<sub>2</sub> SACs (Fig. 4e). For Pt/RuO<sub>2</sub>-700, the oxidation peak between 0.6 and 1.0 V disappeared, showing no MOR activity. The lower MOR performance of these catalysts can be attributed to the Pt aggregation. As is well known, catalytic activity is associated with the number of active sites<sup>29</sup> and single atoms have many more of those compared to clusters or nanoparticles<sup>30</sup>. As expected, due to the presence of Pt clusters or nanoparticles, Pt/RuO<sub>2</sub>-0.75 and Pt/RuO<sub>2</sub>-1.48, two materials with higher Pt loading than Pt<sub>1</sub>/RuO<sub>2</sub> SACs, showed decreased mass activity (Supplementary Fig. 15).

In parallel, an additional sample, denoted as Pt<sub>1</sub>/RuO<sub>2</sub>-H, was prepared by reducing the Pt<sub>1</sub>/RuO<sub>2</sub> SACs in H<sub>2</sub> at 80 °C. In that sample, the RuO<sub>2</sub> support was reduced to metallic Ru with a little RuO<sub>2</sub> left as confirmed by XRD (Supplementary Fig. 16). The different structure led to a changed coordination environment for Pt single atoms. The HAADF-STEM of Pt<sub>1</sub>/RuO<sub>2</sub>-H shows that the Pt atoms are isolated on the support (Fig. 4c). Compared to that of Pt<sub>1</sub>/RuO<sub>2</sub>, the EXAFS spectra of Pt<sub>1</sub>/RuO<sub>2</sub>-H show a prominent peak at 2.49 Å due to Pt-Ru bond (coordination number *n* = 9), and the 1.62 Å peak of Pt-O is negligible (Fig. 4d, Supplementary Fig. 17, and Supplementary Table 1)<sup>31</sup>. These results suggest that the Pt atoms have distinct coordination in Pt<sub>1</sub>/RuO<sub>2</sub> and Pt<sub>1</sub>/RuO<sub>2</sub>-H, i.e., Pt-O coordination for Pt<sub>1</sub>/RuO<sub>2</sub> and Pt-Ru for Pt<sub>1</sub>/RuO<sub>2</sub>-H. Accordingly, the Pt<sub>1</sub>/RuO<sub>2</sub>-H shows no MOR activity (Fig. 4e). Instead, Pt<sub>1</sub>/RuO<sub>2</sub>-H shows enhanced capacitive current and polarization current starting from ~0.9 V in the forward scan, resulting from higher relative Ru content in Pt<sub>1</sub>/RuO<sub>2</sub>-H than Pt<sub>1</sub>/RuO<sub>2</sub>. In consideration of the coordination of Pt-O in Pt<sub>1</sub>/RuO<sub>2</sub> and Pt-C in Pt<sub>1</sub>/VXC-72, it can be concluded that the coordination of Pt single atoms governs MOR activity. On the basis of the preceding results, the origin of MOR activity in Pt<sub>1</sub>/RuO<sub>2</sub> SACs can be attributed to: (i) the existence of large numbers of atomic Pt sites; and (ii) the environment surrounding Pt single atoms (thanks to RuO<sub>2</sub>, Pt single atoms turned into MOR-active catalysts).

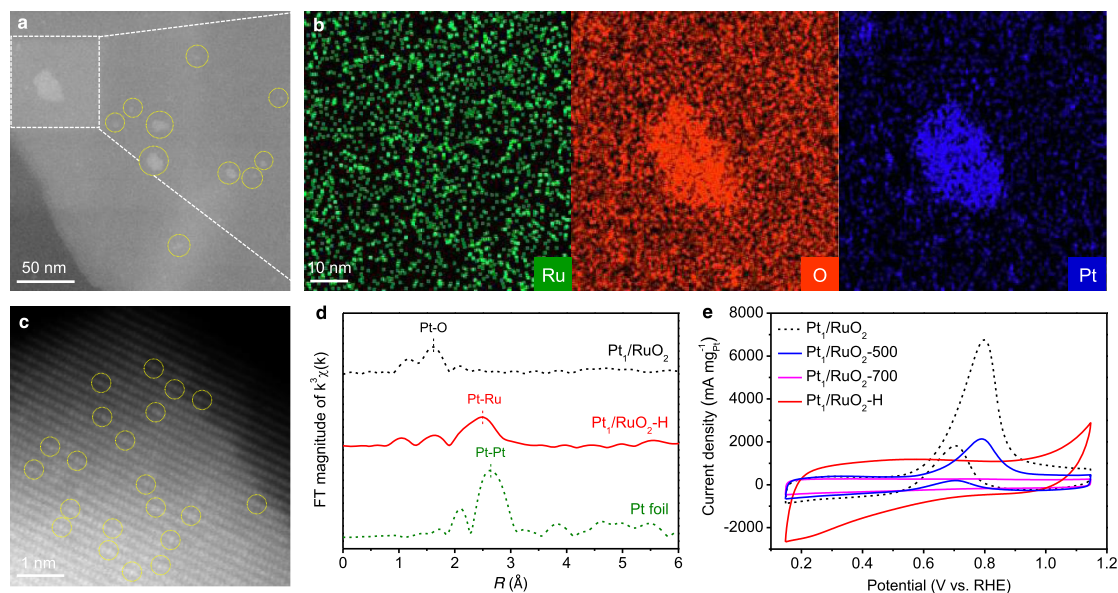


**Fig. 4** Characterizations and MOR performance of  $\text{Pt}_1/\text{RuO}_2\text{-500}/\text{Pt}_1/\text{RuO}_2\text{-700}$  and  $\text{Pt}_1/\text{RuO}_2\text{-H}$  in  $0.1 \text{ mol L}^{-1} \text{ KOH}$  and  $1 \text{ mol L}^{-1}$  methanol solution at a scan rate of  $50 \text{ mV s}^{-1}$ . **a** Typical HAADF-STEM images of  $\text{Pt}_1/\text{RuO}_2\text{-700}$ . **b** Corresponding EDS-mapping images of enlargement in **(a)**. **c** Typical HAADF-STEM images of  $\text{Pt}_1/\text{RuO}_2\text{-H}$ . **d**  $k^3$ -weighted R-space Fourier transformed spectra from EXAFS of  $\text{Pt}_1/\text{RuO}_2\text{-H}$ . **e** MOR performance. The curves in Figs. 2b and 3b are replotted here for convenient comparison.

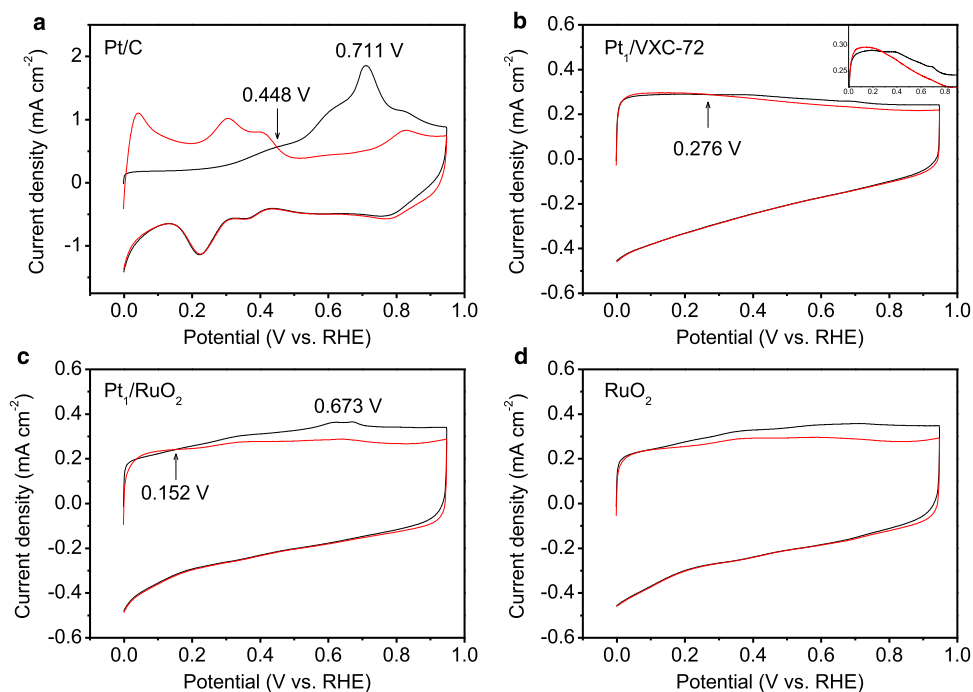


**Fig. 5** CO stripping tests in  $0.1 \text{ mol L}^{-1} \text{ KOH}$  at a scan rate of  $50 \text{ mV s}^{-1}$ . **a** 20 wt% commercial Pt/C. **b**  $\text{Pt}_1/\text{VXC-72}$ . Inset in **(b)** is the local enlargement. **c**  $\text{Pt}_1/\text{RuO}_2$ . **d**  $\text{RuO}_2$ . The black and red curves correspond to the first and second scans, respectively. The first scan was recorded in the presence of CO adsorbed on the electrode, while the second scan was recorded in absence of CO.

The CO resistivity of the catalysts was evaluated by CO stripping tests<sup>6,9</sup>, see Fig. 5. For commercial Pt/C, a main peak appeared in the first forward scan with onset and peak potentials at 0.448 and 0.711 V (Fig. 5a), respectively, where the latter value has been previously attributed to CO electrooxidation taking place on Pt nanoparticles<sup>5</sup>. Downsizing the Pt nanoparticles to the atomic scale in  $\text{Pt}_1/\text{VXC-72}$  reduces the onset potential of CO electrooxidation to  $\sim 0.276 \text{ V}$  (Fig. 5b), a value much lower than that of commercial Pt/C (0.448 V). This reduction indicates that

Pt single atoms trigger CO electrooxidation, consistent with the literature, where Pt single atoms have been shown to weaken CO adsorption, thereby facilitating the oxidation of CO at a lower potential<sup>9</sup>. Compared to  $\text{Pt}_1/\text{VXC-72}$  and commercial Pt/C,  $\text{Pt}_1/\text{RuO}_2$  SACs triggered CO electrooxidation at a lower onset potential of 0.152 V with a minute peak around 0.673 V (Fig. 5c), suggesting an enhanced anti-poisoning capability for  $\text{Pt}_1/\text{RuO}_2$ . Such a change indicates that introducing  $\text{RuO}_2$  as a support favors CO electrooxidation. As is well known, oxophilic  $\text{RuO}_2$

boosts water dissociation, which, in turn, facilitates the formation of adsorbed OH and the oxidative removal of  $\text{CO}_{\text{ads}}$  on Pt sites, which, in turn, facilitates their regeneration<sup>5,6</sup>. As shown in Fig. 5d,  $\text{RuO}_2$  alone electrooxidized CO at a low potential of 0.076 V. Hence, both single atomic Pt and  $\text{RuO}_2$  favor the electrooxidative removal of CO, leading to the superior stability of  $\text{Pt}_1/\text{RuO}_2$ .

Ethanol oxidation reaction (EOR) tests in alkaline medium show an ~5.7-fold higher mass activity of  $\text{Pt}_1/\text{RuO}_2$  compared to benchmark Pt/C (2824 vs. 498  $\text{mA mg}^{-1}_{\text{Pt}}$ ) (Supplementary Fig. 18). These results suggest that  $\text{Pt}_1/\text{RuO}_2$  also has remarkable potential for alcohol oxidation reactions.

**MOR mechanism.** To understand the MOR mechanism, three different models were constructed to simulate the catalytic reaction. The first system had a Pt atom located at the  $\text{Ru}_{\text{cus}}$  (1-fold coordinatively unsaturated Ru) site of the  $\text{RuO}_2(110)$  surface ( $\text{Pt-RuO}_2(110)$ ) corresponding to  $\text{Pt}_1/\text{RuO}_2$ . The second model had a Pt atom bonded to three C atoms on graphene (PtC3) corresponding to  $\text{Pt}_1/\text{VXC-72}$ . The final model had a Pt substituting a surface Ru in  $\text{Ru}(0001)$  ( $\text{Pt-Ru}(0001)$ ) corresponding to  $\text{Pt}_1/\text{RuO}_2\text{-H}$ , see ‘Methods’ and Supplementary Figs. 19–21. The calculated MOR free energy diagrams of these three samples are shown in Fig. 6.

For the MOR on  $\text{Pt-RuO}_2(110)$ , the  $\text{CH}_3\text{OH}$  molecule preferentially adsorbs on the site above  $\text{Ru}_{\text{cus}}$  with a free energy of  $-0.54$  eV (Fig. 6a and Supplementary Fig. 22). Thanks to the highly active  $\text{O}_{\text{br}}$ , the scission of O-H bond of the adsorbed  $\text{CH}_3\text{OH}$  molecule ( $\text{CH}_3\text{OH}^* \rightarrow \text{CH}_3\text{O}^* + \text{H}^*$ ) proceeds spontaneously (Fig. 6a). For this elementary step, the cleaved H atom bonds to its neighboring  $\text{O}_{\text{br}}$  with a reaction free energy of  $-0.26$  eV (Supplementary Fig. 22b and Supplementary Table 3). More importantly, the removal of  $\text{H}^*$  ( $\text{H}^* + \text{OH}^- \rightarrow \text{H}_2\text{O} + \text{e}^-$ ) to leave the sole adsorbate of  $\text{CH}_3\text{O}^*$  is slightly endothermic with a free energy requirement of 0.17 eV at  $\text{pH} = 13$  (Supplementary Table 3). Considering that the O-H bond scission is energetically favorable, we may propose that the MOR starts with the break of the O-H bond in the methanol molecule and follows the  $\text{CH}_3\text{OH}^* \rightarrow \text{CH}_3\text{O}^* \rightarrow \text{CH}_2\text{O}^* \rightarrow \text{CHO}^* \rightarrow \text{CO}^*$  pathway<sup>32,33</sup>.

As illustrated in Fig. 6a, the subsequent activations of the C-H bond require energy barriers of 0.39 ( $\text{CH}_3\text{O}^* \rightarrow \text{TS1} \rightarrow \text{CH}_2\text{O}^*$ ), 0.49 ( $\text{CH}_2\text{O}^* \rightarrow \text{TS2} \rightarrow \text{CHO}$ ), and 0.29 eV ( $\text{CHO}^* \rightarrow \text{TS3} \rightarrow \text{CO}^*$ ), respectively. The dehydrogenation of  $\text{CH}_2\text{O}^*$  has been predicted to be the rate-limiting step for the above-mentioned pathway to CO. This result is consistent with DFT calculations from the Nørskov group showing that MOR on  $\text{RuO}_2(110)$  is limited by the dehydrogenation of  $\text{CH}_2\text{O}^*$ <sup>34</sup>. Nevertheless, the activation barrier on  $\text{Pt-RuO}_2(110)$  was predicted to be only 0.49 eV, which is lower than the 0.71 eV we computed for pure  $\text{RuO}_2(110)$  (Fig. 6a and Supplementary Fig. 23). This barrier reduction can be mainly attributed to the upshift in  $\text{CH}_2\text{O}^*$  energy due to Pt, which lowers the energy difference between the initial and the transition state of TS2. The final dehydrogenation of CHO ( $\text{CHO}^* \rightarrow \text{TS3} \rightarrow \text{CO}^*$ ) was predicted to have a barrier of 0.29 eV, implying that the oxidation of CHO is energetically favored compared to the other two reaction steps ( $\text{CH}_3\text{O}^* \rightarrow \text{TS1} \rightarrow \text{CH}_2\text{O}^*$  and  $\text{CH}_2\text{O}^* \rightarrow \text{TS2} \rightarrow \text{CHO}$ ). The smaller barriers of all the above-mentioned reactions, in particular, the lower barrier of the dehydrogenation of  $\text{CH}_2\text{O}^*$  ( $\text{CH}_2\text{O}^* \rightarrow \text{TS2} \rightarrow \text{CHO}$ ), suggest that the introduction of Pt single atom into  $\text{RuO}_2$  improves the MOR kinetics. Both experimental evidence and DFT simulations support that the  $\text{Pt-O}_{3\text{f}}\text{-Ru}$  configuration together with the  $\text{O}_{\text{br}}$  atoms is the active center, which is responsible for catalyzing the  $\text{CH}_3\text{OH}$  into  $\text{CO}^*$ .

The calculated free energy diagrams for MOR on PtC3 and  $\text{Pt-Ru}(0001)$  are shown in Fig. 6b, c for comparison. The adsorption free energy of  $\text{CH}_3\text{OH}$  on the PtC3 and  $\text{Pt-Ru}(0001)$  are  $-0.03$  and 0.15 eV, respectively. Both values are less negative than that computed for  $\text{Pt-RuO}_2(110)$  ( $-0.54$  eV), implying a weaker interaction between both PtC3 and  $\text{Pt-Ru}(0001)$  and the methanol molecule in comparison to  $\text{Pt-RuO}_2(110)$ . Moreover, the energy barriers needed to cleave the O-H and C-H bonds are significantly higher than those of  $\text{Pt-RuO}_2(110)$  (Fig. 6a–c). The much higher barriers compared to those on  $\text{Pt-RuO}_2(110)$  indicate that the MOR is energetically costly for both PtC3 and  $\text{Pt-Ru}(0001)$  substrates. These computational results agree with experiments as both suggest that  $\text{Pt}_1/\text{VXC-72}$  and  $\text{Pt}_1/\text{RuO}_2\text{-H}$  are inert towards MOR. As for  $\text{Pt-RuO}_2(101)$ , the highest reaction activation barrier (0.79 eV) is much lower than that of both PtC3

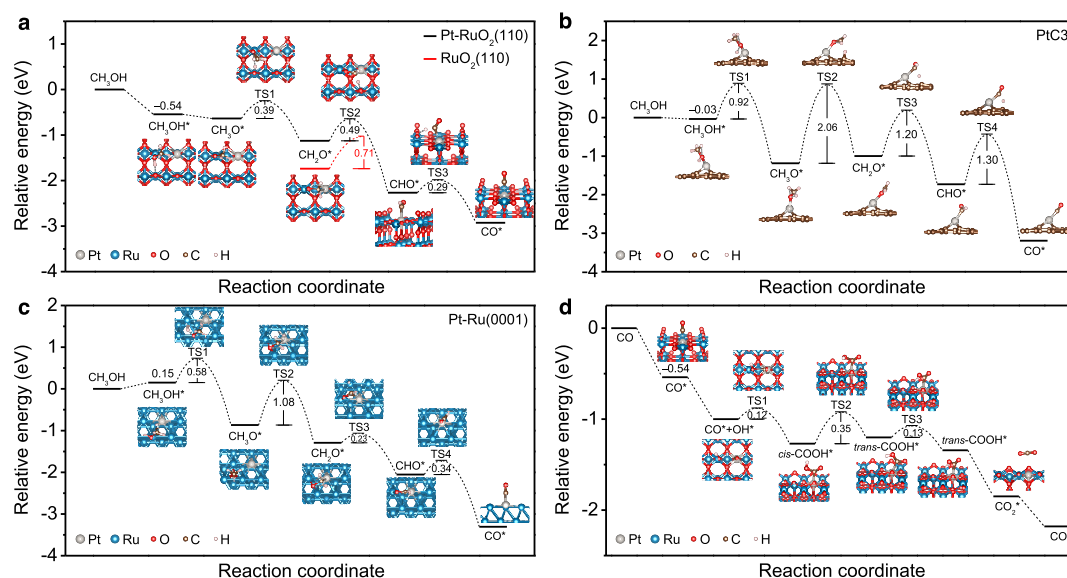


**Fig. 6** MOR mechanism. **a–c** Calculated reaction free energy and energy barriers for methanol oxidation to CO at: **a**  $\text{Pt-RuO}_2(110)$ , **b** PtC3, and **c**  $\text{Pt-Ru}(0001)$ . **d** Calculated reaction free energy and energy barriers for CO oxidation on  $\text{Pt-RuO}_2(110)$ . In **(a)**, the relative energies of  $\text{CH}_2\text{O}^*$  and corresponding TS2 computed for  $\text{RuO}_2(110)$  are shown for reference.

(2.06 eV) and Pt-Ru(0001) (1.08 eV) (Supplementary Fig. 24 and Fig. 6b, c), suggesting the enhanced activity of Pt<sub>1</sub>/RuO<sub>2</sub> compared to Pt<sub>1</sub>/VXC-72 and Pt<sub>1</sub>/RuO<sub>2</sub>-H towards MOR.

We also theoretically studied the stability of Pt-RuO<sub>2</sub>(110) with respect to CO poisoning, or equivalently, the oxidation of CO into CO<sub>2</sub>. When OH\* is present, CO oxidation proceeds through the CO\* + OH\* → TS1 → *cis*-COOH\* → TS2 → *trans*-COOH\* → TS3 → *trans*-COOH\* → CO<sub>2</sub>\* pathway<sup>35</sup>, as shown in Fig. 6d. The rate-limiting step of the overall reaction was predicted to be the *cis*-COOH\* → *trans*-COOH\* step (i.e., the rotation of the H atom in *cis*-COOH\*) with activation barrier of 0.35 eV. This value is even smaller than the barrier computed for the dehydrogenation of formaldehyde on Pt-RuO<sub>2</sub>(110), implying that the presence of Pt facilitates the full oxidation of methanol into CO<sub>2</sub> on RuO<sub>2</sub>(110). We further note that the *trans*-COOH\* → CO<sub>2</sub>\* step (i.e., the desorption of CO<sub>2</sub>\*) has a positive ΔG of 0.33 eV, indicating that the release of CO<sub>2</sub> is spontaneous. It is worth mentioning that the adsorption free energies of CO on the PtC3 and Pt-Ru(0001) are -0.81 and -0.92 eV (Fig. 6b, c), respectively. Both values are much more negative compared to that computed for Pt-RuO<sub>2</sub>(110) (-0.54 eV), suggesting an increased interaction between CO and the PtC3/Pt-Ru(0001). According to the Brønsted-Evans-Polanyi relationship<sup>36,37</sup>, higher binding energy correlates to higher activation energies and lower thermodynamic driving force for the reaction. Therefore, we predict that the CO electrooxidation on PtC3 and Pt-Ru(0001) is much more energetically unfavorable with sluggish kinetics in agreement with the experiments above.

In addition to the activation energy barriers, onset potentials were also calculated (Supplementary Fig. 25). The potential-determining step (i.e., the elementary step with the highest onset potential) was found to be, for all three catalysts, the stripping off methoxyl proton (CH<sub>3</sub>O\* → CH<sub>2</sub>O\*). Accordingly, the onset potentials were predicted to be 0.26, 0.92, and 0.33 V for Pt-RuO<sub>2</sub>(110), PtC3, and Pt-Ru(0001), respectively. Both the lower onset potential and smaller activation barriers suggest that Pt<sub>1</sub>/RuO<sub>2</sub> SACs are more favorable towards the methanol oxidation than Pt<sub>1</sub>/VXC-72 and Pt<sub>1</sub>/RuO<sub>2</sub>-H, in agreement with experimental results.

To unravel the mechanisms underpinning the high MOR activity, we calculated the projected density of states (PDOS) and charge analysis for both Pt and Ru<sub>cus</sub> atoms in the Pt-RuO<sub>2</sub>(110). It is apparent that only the spin-up state of the *dz*<sup>2</sup> orbital of Pt is filled while the *dz*<sup>2</sup> orbital of Ru<sub>cus</sub> is empty (Supplementary Fig. 26). Consistent with the PDOS results, the charge density difference also suggests that more electrons are depleted for the Ru<sub>cus</sub> than the Pt atom (Supplementary Fig. 27). Specifically, Bader charge analysis suggests that Ru<sub>cus</sub> and Pt on Pt-RuO<sub>2</sub>(110) lose 1.61 e and 1.22 e, respectively (Supplementary Table 4). Thanks to the empty anti-bonding *dz*<sup>2</sup> orbital, a stronger interaction between the adsorbate (e.g., CH<sub>3</sub>OH) and Ru<sub>cus</sub> than that of Pt is predicted, in agreement with the calculated adsorption free energies (Supplementary Fig. 22a–c). The orbital interaction between adsorbate, e.g., CH<sub>3</sub>OH, and the *dz*<sup>2</sup> orbital is shown in Supplementary Fig. 28. In the case of Ru<sub>cus</sub>, for which the *dz*<sup>2</sup> orbital is empty, the methanol molecule is well stabilized due to the favorable two-center two-electron interaction. Instead, the anti-bonding *dz*<sup>2</sup> orbital of Pt is filled with one spin-up electron, resulting in the less-favorable two-center three-electron interaction, thereby destabilizing the adsorbate. Specifically, the filled anti-bonding Pt orbital leads to a weaker adsorption free energy of formaldehyde on Pt-RuO<sub>2</sub>(110) (-0.26 eV) compared to that of RuO<sub>2</sub>(110) (-0.88 eV) (Fig. 6a). The increased energy towards CH<sub>2</sub>O\* thus lowers the activation barrier (TS2) for the subsequent dehydrogenation (Fig. 6a). We further evaluated the PDOS of the *d* orbitals with a Pt atom placed on different substrates. Compared to Pt-Ru(0001), the *d* orbitals of Pt on Pt-RuO<sub>2</sub>(110) are characterized

by greater delocalization (Supplementary Fig. 29)<sup>32</sup> as well as a larger density near the Fermi level. These features facilitate electron transfer and contribute to the enhanced MOR activity of Pt<sub>1</sub>/RuO<sub>2</sub><sup>35</sup>. In contrast, the Pt PDOS of PtC3 is small at the Fermi level (Supplementary Fig. 29), suggesting that Pt<sub>1</sub>/VXC-72 is an ineffective MOR catalyst<sup>9</sup>. Besides, the additional *d* electrons in the Pt of PtC3 and Pt-Ru(0001) cause stronger repulsion to the coming ligand, e.g., CH<sub>3</sub>OH, thus weakening the adsorption of methanol and hindering MOR.

## Discussion

We successfully prepared Pt single atoms characterized by distinct coordination environment by leveraging a simple impregnation–adsorption method and tailoring the support. The Pt<sub>1</sub>/RuO<sub>2</sub> SACs not only had a superb mass activity of 6766 mA mg<sup>-1</sup><sub>Pt</sub> but also CO resistibility towards the MOR. Pt<sub>1</sub>/RuO<sub>2</sub> was shown to be a significantly better catalyst compared to the commercial Pt/C benchmark. Theoretical simulations revealed that the Pt-O<sub>3f</sub>-Ru<sub>cus</sub> with O<sub>br</sub> in Pt<sub>1</sub>/RuO<sub>2</sub> favored dehydrogenation of methanol with a low energy barrier and onset potential compared to that of Pt-C and Pt-Ru bonds. Moreover, CO at Pt<sub>1</sub>/RuO<sub>2</sub> can be removed via electrooxidation at low potentials, leading to enhanced anti-poisoning capability. The discovery of Pt<sub>1</sub>/RuO<sub>2</sub> SACs provides an approach to explore Pt SACs for MOR and related alcohol oxidation reaction.

## Methods

**Materials.** H<sub>2</sub>PtCl<sub>6</sub>·6H<sub>2</sub>O, RuO<sub>2</sub>, and commercial Pt/C (20 wt% Pt) were purchased from Sigma-Aldrich. Carbon black (Vulcan XC-72) was bought from The Cabot Corporation. Methanol and ethanol were purchased from Scharlab.

**Synthesis of Pt<sub>1</sub>/RuO<sub>2</sub> and control catalysts.** The Pt<sub>1</sub>/RuO<sub>2</sub> catalysts were prepared by an impregnation–adsorption method. Briefly, 50 mg of RuO<sub>2</sub> were dispersed in 80 mL of distilled water. Next, 0.25 mL of a H<sub>2</sub>PtCl<sub>6</sub>·6H<sub>2</sub>O solution (2 mg mL<sup>-1</sup>) was added dropwise; stirring at 70 °C for 5 h followed this. The product was obtained by filtration, repeated washing with water and ethanol, and drying at 70 °C overnight. Pt<sub>1</sub>/VXC-72 was prepared in a similar manner by using VXC-72. Pt<sub>1</sub>/RuO<sub>2</sub>-H catalyst was obtained by reducing Pt<sub>1</sub>/RuO<sub>2</sub> in H<sub>2</sub> at 80 °C. The Pt<sub>1</sub>/RuO<sub>2</sub>-500 and Pt<sub>1</sub>/RuO<sub>2</sub>-700 catalysts were obtained under the heat treatment of Pt<sub>1</sub>/RuO<sub>2</sub> in the air at 500 and 700 °C, respectively.

**Catalyst characterization.** The structure and morphology of the catalysts were characterized by XRD (PANalytical X'pert Pro, Cu Kα radiation), XPS (Axis Ultra DLD), and TEM (JEOL-2010F). The electron paramagnetic resonance (EPR) spectra were recorded at room temperature by using JEOL JES-FA200. The HAADF-STEM and EDS mapping were carried out using a double Cs-corrected FEI-Themis microscope operated at 300 kV. The STEM images were obtained with a convergent semi-angle of 25.1 mrad. The HAADF collection angle was 48–200 mrad. The XAFS at the Pt L<sub>3</sub>-edge was obtained on beamline 10C at the Pohang Light Source (PLS) in the Pohang Accelerator Laboratory (PAL), Republic of Korea. The XAFS data were processed and analyzed using ATHENA and ARTEMIS<sup>38</sup>. The Pt content in the catalyst was measured by ultraviolet visible spectroscopy (UV-vis, Lambda 20, Perkin Elmer). An appropriate amount of a H<sub>2</sub>PtCl<sub>6</sub>·6H<sub>2</sub>O solution (2 mg mL<sup>-1</sup>) was added to deionized water and diluted to 100 mL. After the adsorption of Pt species by RuO<sub>2</sub> in solution, the residual solution was measured by UV-vis, and by the comparison of the absorbance with the working curve, the Pt content in RuO<sub>2</sub> was estimated.

**Electrochemical characterization.** The electrochemical tests were conducted using a CHI 900D workstation (CH Instruments). A three-electrode setup was used and all tests were conducted at 25 °C. A graphite rod was used as a counter electrode; (KCl saturated) Ag/AgCl was selected as the reference electrode. To prepare the working electrode, 1 mg of catalyst and 1 mg of VXC-72 were ultrasonically dispersed in a mixture of 200 μL of water, 50 μL of ethanol, and 20 μL of Nafion (Dupont, 5 wt%). Next, 5 μL of the above ink was then placed onto a glassy-carbon electrode (4 mm in diameter) and dried at room temperature. In an N<sub>2</sub>-purged 0.1 mol L<sup>-1</sup> KOH and 1 mol L<sup>-1</sup> methanol/ethanol solution, the MOR/EOR electrocatalytic activity was evaluated by CV (scan rate was set at 50 mV s<sup>-1</sup>). CV scans were performed until a convergent response was recorded. For the CO stripping tests, CO was adsorbed on the catalyst by bubbling CO in 0.1 mol L<sup>-1</sup> KOH for 10 min at a potential of -0.95 V vs. Ag/AgCl. CO in the solution was eliminated by bubbling the electrolyte with N<sub>2</sub> for 20 min. Stripping tests were carried out from -0.95 to 0 V at 50 mV s<sup>-1</sup> for two consecutive scans.

All measured potentials were converted to the RHE using

$$E_{\text{RHE}} = E_{\text{Ag/AgCl}} + 0.198 + 0.059 \times \text{pH}.$$

### Computational details

**Models.** The RuO<sub>2</sub> substrate was modeled by the  $p(3 \times 1)$  unit cell of RuO<sub>2</sub>(110) in a six-layered slab with 18 Ru atoms and 36 O atoms. The RuO<sub>2</sub>(110) was chosen because this surface has previously been reported to have the most thermodynamically favorable free energy during most synthesis procedures<sup>34,39,40</sup>. The RuO<sub>2</sub>(110) surface was constructed from the relaxed RuO<sub>2</sub> bulk in the P4<sub>2</sub>/mnm space group, which has a lattice constant of  $a = b = 4.52 \text{ \AA}$  and  $c = 3.12 \text{ \AA}$ <sup>41</sup>. For a stoichiometric RuO<sub>2</sub>(110) surface, there are several different sites, i.e., the 1-fold coordinatively unsaturated Ru (Ru<sub>cus</sub>), the coordinatively saturated Ru (Ru<sub>sat</sub>), the undercoordinated bridging O (O<sub>br</sub>), and the 3-fold coordinatively bonded O (O<sub>3f</sub>) (Supplementary Fig. 19a). Among these sites, Ru<sub>cus</sub> and O<sub>br</sub> are widely believed to be catalytically active for chemical reactions<sup>41,42</sup>. To simulate the Pt<sub>1</sub>/RuO<sub>2</sub>, two different structures with one Pt atom located at either the Ru<sub>cus</sub> or the Ru<sub>sat</sub> of RuO<sub>2</sub>(110) were considered (Supplementary Fig. 19b). It was noticed that the Pt at the Ru<sub>cus</sub> shows lower energy by 0.21 eV compared to that at the Ru<sub>sat</sub>, implying that the single Pt atom favors the Ru<sub>cus</sub> (Supplementary Fig. 19b). A 5 × 5 graphene sheet and a five-layered slab of  $p(3 \times 3)$  unit cell Ru(0001) were constructed to simulate the VXC-72 and the Ru substrate, respectively. One C atom in the graphene sheet and one top layer Ru atom in the Ru(0001) slab were replaced by the Pt to model the Pt<sub>1</sub>/VXC-72 and Pt<sub>1</sub>/RuO<sub>2</sub>-H, respectively (Supplementary Figs. 20 and 21). A vacuum space of 15 Å along the  $c$  direction was added for all substrates to avoid strong interactions between neighboring substrates.

**DFT calculations.** All the spin-polarized first-principle calculations were performed using the Vienna Ab initio Simulation Package (VASP)<sup>43,44</sup> with a plane-wave basis set defined by a kinetic energy cutoff 400 eV. The projector augmented wave (PAW)<sup>45</sup> pseudopotentials with valence-electron configurations of 2s<sup>2</sup>2p<sup>2</sup>, 2s<sup>2</sup>2p<sup>4</sup>, 1s<sup>1</sup>, 4p<sup>6</sup>4d<sup>7</sup>5s<sup>1</sup>, and 5d<sup>9</sup>6s<sup>1</sup> were employed for C, O, H, Ru, and Pt, respectively. The electron exchange-correlation was described using the Perdew-Burk-Ernzerhof (PBE)<sup>46</sup> functional under the generalized gradient approximation (GGA) scheme. For all the calculations, a dipole correction along the  $c$  direction was also applied. The bottom three layers of the RuO<sub>2</sub>(110) and the Ru(0001) slabs were fixed during the relaxation, whereas the top three layers were fully relaxed until the energy and force converged within 10<sup>-5</sup> eV and 0.02 eV Å<sup>-1</sup>, respectively. The Brillouin zones were sampled using Gamma centered  $k$ -points with spacing smaller than  $2\pi \times 0.04 \text{ \AA}^{-1}$ .

The binding energy of one Pt atom with the substrate was evaluated as  $E_{\text{bind}} = E(\text{Pt-sub}) - E(\text{Pt}) - E(\text{sub})$ , where  $E(\text{Pt-sub})$  and  $E(\text{sub})$  are the energies of the system with one Pt atom and the pure substrate, respectively, and  $E(\text{Pt})$  is the total energy per atom for Pt bulk metal. The transition states (TSs) were located by the combination of both the nudged elastic band (NEB) method and the dimer method<sup>47-49</sup>. All the TSs were confirmed by noticing only one imaginary vibrational frequency. The adsorption energy of the intermediate was calculated by  $\Delta E_{\text{ads}} = E(\text{adsorbate-sub}) - E(\text{sub}) - E(\text{adsorbate})$ , where  $E(\text{adsorbate-sub})$  is the energy of the system with the adsorbate on the substrate,  $E(\text{sub})$  is the energy of the clean substrate, and  $E(\text{adsorbate})$  is the energy of the isolated adsorbate molecule in the vacuum. The adsorption free energy was further calculated as  $\Delta G_{\text{ads}} = \Delta E_{\text{ads}} + \Delta \text{ZPE} - T\Delta S$ , where  $\Delta \text{ZPE}$  is the change of zero-point energies, and  $\Delta S$  is the entropy difference, and  $T$  is the temperature (298.15 K). The activation energy was calculated as  $E_a = E(\text{TS}) - E(\text{IS})$ , where  $E(\text{TS})$  and  $E(\text{IS})$  are the energies for the TS and the initial state (IS).

The change in Gibbs free energy ( $\Delta G$ ) for all the reaction steps were calculated based on the method developed by Nørskov et al.<sup>50</sup> At experimental condition ( $U = 0$ , pH,  $p = 1$  bar,  $T = 298$  K), the free energy  $\Delta G$  is calculated as  $\Delta G = \Delta E + \Delta \text{ZPE} - T\Delta S + \Delta G_{\text{pH}}$ , where  $\Delta E$  is the energy difference by DFT calculations, and  $\Delta G_{\text{pH}}$  corresponds to the correction due to the pH that is different from 0, i.e.,  $\Delta G_{\text{pH}} = -k_{\text{B}}T \ln[\text{H}^+] = 0.0592 \text{ pH}$ . The free energy of OH<sup>-</sup> was calculated by  $G(\text{OH}^-) = G(\text{H}_2\text{O}(\text{l})) - G(\text{H}^+) = G(\text{H}_2\text{O}(\text{l})) - G(\text{H}_2(\text{g}))/2$ <sup>51</sup>, where  $G(\text{H}_2\text{O}(\text{l}))$  is the Gibbs free energy of one water molecule under the saturated vapor pressure (0.035 bar), and  $G(\text{H}^+)$  is taken as half of  $G(\text{H}_2(\text{g}))$ , i.e., the free energy of H<sub>2</sub>(g) at standard condition ( $p = 1$  bar,  $T = 298$  K).

The computational standard hydrogen electrode was used to calculate the onset potentials<sup>33,50</sup>. Under this framework, the influence of the applied potential  $U$  was computed by adding  $\Delta G_U = -eU$  to the free energy of a reaction involving the formation of a proton–electron pair. The electrochemical potential pertaining to each elementary step was calculated using  $U_i = \Delta G_i/e$ , where  $\Delta G_i$  is the reaction free energy calculated according to Supplementary Table 5. The overall onset potential was estimated as  $U_{\text{onset}} = \max(\Delta G_i/e)$ <sup>33</sup>.

### Data availability

All the raw data used in this work are available on reasonable request from the corresponding author.

Received: 7 December 2020; Accepted: 30 July 2021;

Published online: 02 September 2021

### References

- Kakati, N. et al. Anode catalysts for direct methanol fuel cells in acidic media: do we have any alternative for Pt or Pt–Ru? *Chem. Rev.* **114**, 12397–12429 (2014).
- Zhao, X. et al. Recent advances in catalysts for direct methanol fuel cells. *Energy Environ. Sci.* **4**, 2736–2753 (2011).
- Chen, S. et al. High-performance Pt–Co nanoframes for fuel-cell electrocatalysis. *Nano Lett.* **20**, 1974–1979 (2020).
- Huang, J. et al. PtCuNi tetrahedra catalysts with tailored surfaces for efficient alcohol oxidation. *Nano Lett.* **19**, 5431–5436 (2019).
- Huang, W. et al. Highly active and durable methanol oxidation electrocatalyst based on the synergy of platinum–nickel hydroxide–graphene. *Nat. Commun.* **6**, 10035 (2015).
- Zhang, Z. et al. Efficient ternary synergism of platinum/tin oxide/nitrogen-doped carbon leading to high-performance ethanol oxidation. *ACS Catal.* **8**, 8477–8483 (2018).
- Wang, X. et al. Bismuth oxyhydroxide–Pt inverse interface for enhanced methanol electrooxidation performance. *Nano Lett.* **20**, 7751–7759 (2020).
- Zhao, D. et al. Atomic site electrocatalysts for water splitting, oxygen reduction and selective oxidation. *Chem. Soc. Rev.* **49**, 2215–2264 (2020).
- Xiong, Y. et al. Single-atom Rh/N-doped carbon electrocatalyst for formic acid oxidation. *Nat. Nanotechnol.* **15**, 390–397 (2020).
- Li, Z. et al. Iridium single-atom catalyst on nitrogen-doped carbon for formic acid oxidation synthesized using a general host–guest strategy. *Nat. Chem.* **12**, 764–772 (2020).
- Zhang, Z. et al. Atomically dispersed materials for rechargeable batteries. *Nano Energy* **76**, 105085 (2020).
- Wang, Q. et al. Ultrahigh-loading of Ir single atoms on NiO matrix to dramatically enhance oxygen evolution reaction. *J. Am. Chem. Soc.* **142**, 7425–7433 (2020).
- Qiao, B. et al. Single-atom catalysis of CO oxidation using Pt<sub>1</sub>/FeO<sub>x</sub>. *Nat. Chem.* **3**, 634–641 (2011).
- Cuesta, A. At least three contiguous atoms are necessary for CO formation during methanol electrooxidation on platinum. *J. Am. Chem. Soc.* **128**, 13332–13333 (2006).
- Kim, Y.-T. et al. Fine size control of platinum on carbon nanotubes: from single atoms to clusters. *Angew. Chem. Int. Ed.* **45**, 407–411 (2006).
- Qin, R., Liu, K., Wu, Q. & Zheng, N. Surface coordination chemistry of atomically dispersed metal catalysts. *Chem. Rev.* **120**, 11810–11899 (2020).
- Zhang, J. et al. Tuning the coordination environment in single-atom catalysts to achieve highly efficient oxygen reduction reactions. *J. Am. Chem. Soc.* **141**, 20118–20126 (2019).
- Tang, C. et al. Coordination tunes selectivity: two-electron oxygen reduction on high-loading molybdenum single-atom catalysts. *Angew. Chem. Int. Ed.* **59**, 9171–9176 (2020).
- Li, S. et al. Impact of the coordination environment on atomically dispersed Pt catalysts for oxygen reduction reaction. *ACS Catal.* **10**, 907–913 (2020).
- Gong, Y.-N. et al. Regulating the coordination environment of MOF-templated single-atom nickel electrocatalysts for boosting CO<sub>2</sub> reduction. *Angew. Chem. Int. Ed.* **59**, 2705–2709 (2020).
- Zhang, Z. et al. The simplest construction of single-site catalysts by the synergism of micropore trapping and nitrogen anchoring. *Nat. Commun.* **10**, 1657 (2019).
- Chen, Y. et al. Engineering the atomic interface with single platinum atoms for enhanced photocatalytic hydrogen production. *Angew. Chem. Int. Ed.* **59**, 1295–1301 (2020).
- Zhou, K. L. et al. Seamlessly conductive Co(OH)<sub>2</sub> tailored atomically dispersed Pt electrocatalyst with a hierarchical nanostructure for an efficient hydrogen evolution reaction. *Energy Environ. Sci.* **13**, 3082–3092 (2020).
- Yoshida, H., Nonoyama, S. & Hattori, Y. Y. T. Quantitative determination of platinum oxidation state by XANES analysis. *Phys. Scr.* **T115**, 813–815 (2005).
- Cao, L. et al. Dynamic oxygen adsorption on single-atomic ruthenium catalyst with high performance for acidic oxygen evolution reaction. *Nat. Commun.* **10**, 4849 (2019).
- Huang, Z.-F. et al. Chemical and structural origin of lattice oxygen oxidation in Co–Zn oxyhydroxide oxygen evolution electrocatalysts. *Nat. Energy* **4**, 329–338 (2019).
- Zhu, C., Fu, S., Shi, Q., Du, D. & Lin, Y. Single-atom electrocatalysts. *Angew. Chem. Int. Ed.* **56**, 13944–13960 (2017).
- Zhang, W. et al. Ultrathin PtNiM (M = Rh, Os, and Ir) nanowires as efficient fuel oxidation electrocatalytic materials. *Adv. Mater.* **31**, 1805833 (2019).
- Seh, Z. W. et al. Combining theory and experiment in electrocatalysis: insights into materials design. *Science* **355**, eaad4998 (2017).
- Liu, M. et al. Atomically dispersed metal catalysts for the oxygen reduction reaction: synthesis, characterization, reaction mechanisms and electrochemical energy applications. *Energy Environ. Sci.* **12**, 2890–2923 (2019).

31. Zhang, L. et al. Atomic layer deposited Pt–Ru dual-metal dimers and identifying their active sites for hydrogen evolution reaction. *Nat. Commun.* **10**, 4936 (2019).
32. Zhao, L. et al. The oxidation of methanol on PtRu(111): a periodic density functional theory investigation. *J. Phys. Chem. C* **119**, 20389–20400 (2015).
33. Ferrin, P. & Mavrikakis, M. Structure sensitivity of methanol electrooxidation on transition metals. *J. Am. Chem. Soc.* **131**, 14381–14389 (2009).
34. Latimer, A. A., Abild-Pedersen, F. & Nørskov, J. K. A theoretical study of methanol oxidation on RuO<sub>2</sub>(110): bridging the pressure gap. *ACS Catal.* **7**, 4527–4534 (2017).
35. Wang, X. et al. Materializing efficient methanol oxidation via electron delocalization in nickel hydroxide nanoribbon. *Nat. Commun.* **11**, 4647 (2020).
36. Evans, M. G. & Polanyi, M. Further considerations on the thermodynamics of chemical equilibria and reaction rates. *Trans. Faraday Soc.* **32**, 1333–1360 (1936).
37. Bronsted, J. N. Acid and basic catalysis. *Chem. Rev.* **5**, 231–338 (1928).
38. Ravel, B. & Newville, M. ATHENA, ARTEMIS, HEPHAESTUS: data analysis for X-ray absorption spectroscopy using IFEFFIT. *J. Synchrotron Radiat.* **12**, 537–541 (2005).
39. Wang, T., Jelic, J., Rosenthal, D. & Reuter, K. Exploring pretreatment–morphology relationships: ab initio wulff construction for RuO<sub>2</sub> nanoparticles under oxidising conditions. *ChemCatChem* **5**, 3398–3403 (2013).
40. Wang, H. & Schneider, W. F. Effects of coverage on the structures, energetics, and electronics of oxygen adsorption on RuO<sub>2</sub>(110). *J. Chem. Phys.* **127**, 064706 (2007).
41. Over, H. et al. Atomic-scale structure and catalytic reactivity of the RuO<sub>2</sub>(110) surface. *Science* **287**, 1474–1476 (2000).
42. Knapp, M. et al. Complex interaction of hydrogen with the RuO<sub>2</sub>(110) surface. *J. Phys. Chem. C* **111**, 5363–5373 (2007).
43. Kresse, G. & Furthmüller, J. Efficient iterative schemes for ab initio total-energy calculations using a plane-wave basis set. *Phys. Rev. B* **54**, 11169–11186 (1996).
44. Kresse, G. & Furthmüller, J. Efficiency of ab-initio total energy calculations for metals and semiconductors using a plane-wave basis set. *Comput. Mater. Sci.* **6**, 15–50 (1996).
45. Blöchl, P. E. Projector augmented-wave method. *Phys. Rev. B* **50**, 17953–17979 (1994).
46. Perdew, J. P., Burke, K. & Ernzerhof, M. Generalized gradient approximation made simple. *Phys. Rev. Lett.* **77**, 3865–3868 (1996).
47. Henkelman, G. & Jónsson, H. A dimer method for finding saddle points on high dimensional potential surfaces using only first derivatives. *J. Chem. Phys.* **111**, 7010–7022 (1999).
48. Henkelman, G. & Jónsson, H. Improved tangent estimate in the nudged elastic band method for finding minimum energy paths and saddle points. *J. Chem. Phys.* **113**, 9978–9985 (2000).
49. Henkelman, G., Uberuaga, B. P. & Jónsson, H. A climbing image nudged elastic band method for finding saddle points and minimum energy paths. *J. Chem. Phys.* **113**, 9901–9904 (2000).
50. Nørskov, J. K. et al. Origin of the overpotential for oxygen reduction at a fuel-cell cathode. *J. Phys. Chem. B* **108**, 17886–17892 (2004).
51. Jiao, Y., Zheng, Y., Jaroniec, M. & Qiao, S. Z. Origin of the electrocatalytic oxygen reduction activity of graphene-based catalysts: a roadmap to achieve the best performance. *J. Am. Chem. Soc.* **136**, 4394–4403 (2014).

## Acknowledgements

This work was jointly supported by the Research Grants Council of Hong Kong (GRF Projects: 16201820 and 16206019), the Guangzhou Science and Technology Program (No. 201807010074), and the Science and Technology Planning Project of Guangdong Province, China (2017A050506014). M.G. and Q.W. acknowledge funding from the Guangdong Provincial Key Laboratory of Energy Materials for Electric Power with project no. 2018B030322001, Guangdong Innovative and Entrepreneurial Research Team Program (2016ZT06N500), Shenzhen Peacock Plan (KQTD2016022620054656), Shenzhen Clean Energy Research Institute (No. CERI-KY-2019-003). The authors also acknowledge the technical assistance from the Materials Characterization and Preparation Facilities (MCPF) of HKUST.

## Author contributions

F.C. supervised the project. Z.Q.Z. conceived the idea, designed and performed the experiments. J.P.L. carried out the DFT calculations. J.W. and J.L. did the XAFS characterizations. Q.W. and M.G. performed the HAADF-STEM measurements. K.W. and Z.H.T. helped with the XPS measurements. Y.H.W. did the UV-vis measurements. Z.Q.Z., J.P.L., and F.C. wrote the manuscript. T.S.Z. commented on the manuscript. All the authors contributed to the manuscript.

## Competing interests

The authors declare no competing interests.

## Additional information

**Supplementary information** The online version contains supplementary material available at <https://doi.org/10.1038/s41467-021-25562-y>.

**Correspondence** and requests for materials should be addressed to F.C.

**Peer review information** *Nature Communications* thanks the reviewer(s) for their contribution to the peer review of this work.

**Reprints and permission information** is available at <http://www.nature.com/reprints>

**Publisher's note** Springer Nature remains neutral with regard to jurisdictional claims in published maps and institutional affiliations.



**Open Access** This article is licensed under a Creative Commons Attribution 4.0 International License, which permits use, sharing, adaptation, distribution and reproduction in any medium or format, as long as you give appropriate credit to the original author(s) and the source, provide a link to the Creative Commons license, and indicate if changes were made. The images or other third party material in this article are included in the article's Creative Commons license, unless indicated otherwise in a credit line to the material. If material is not included in the article's Creative Commons license and your intended use is not permitted by statutory regulation or exceeds the permitted use, you will need to obtain permission directly from the copyright holder. To view a copy of this license, visit <http://creativecommons.org/licenses/by/4.0/>.

© The Author(s) 2021